Available online at www.sciencedirect.com
ScienceDirect
Trans. Nonferrous Met. Soc. China 34(2024) 1251−1262
Transactions of Nonferrous Metals Society of China
www.tnmsc.cn

Effects of W-doping on precursor growth of $LiNi_{0.88}Co_{0.09}Mn_{0.03}O_2$ and its electrochemical performance

Lei CHENG[1,2#], Yi ZHAO[3#], Bin HUANG[1], Zao-wen ZHAO[4], Yan-wei LI[1], Wei LI[1]

1. Guangxi Key Laboratory of Electrochemical and Magneto-chemical Functional Materials,
College of Chemistry and Bioengineering, Guilin University of Technology, Guilin 541004, China;
2. Zhejiang Power New Energy Co., Ltd., Zhuji 311899, China;
3. School of Metallurgy and Environment, Central South University, Changsha 410083, China;
4. School of Materials Science and Engineering, Hainan University, Haikou 570228, China

Received 10 October 2022; accepted 5 May 2023

Abstract: W-doped $LiNi_{0.88}Co_{0.09}Mn_{0.03}O_2$ cathodes were fabricated by using W-doped precursors. X-ray diffraction indicates that W-doping suppresses the crystal growth of the precursor along the direction perpendicular to *c*-axis. Scanning electron microscopy results show that the primary particles of the cathode become finer with the increase of W-doping amount. Electrochemical measurements prove the merits of the W-doped cathodes. The one with 0.4 wt.% W-doping shows significantly improved electrochemical properties compared with the pristine one. After 100 charge−discharge cycles at a high rate of 10*C*, it exhibits capacity retentions of 94.68% and 89.63% at 25 and 45 °C, respectively. The intergranular cracks after cycles are also suppressed by W-doping. Hence, profiting from the synergistic effect of component regulation and microstructure engineering by W-doping, the Li^+ diffusion kinetics is boosted, and the structural stability is enhanced.

Key words: W-doping; precursor growth; structural stability; cycle life; lithium-ion batteries

1 Introduction

Nowadays, with the rapid development of consumer electronics, portable power tools and electric vehicles (EVs), next generation cathode materials with high energy-density, low cost, high reliability and long cycle life for lithium-ion batteries (LIBs) are urgently needed [1,2]. In the past decades, layered $LiNi_xCo_yMn_zO_2$ (NCM, $x+y+z=1$) oxides have gradually become one of the mainstream cathode materials due to high capacity, high electronic conductivity and outstanding structural stability [3]. More importantly, the specific capacity can be feasibly enhanced by increasing Ni content. Therefore, in recent years, Ni-rich NCM ($x \geq 0.8$) materials have attracted wide attentions in the field of EVs due to their high specific capacity of over 200 mA·h/g [4,5].

Although Ni-rich NCM cathodes possess high energy-density, the large-scale application of Ni-rich cathode materials is still hindered by the following issues: (1) The cation disordering (i.e., the occupation of Li sites by Ni^{2+} ions) due to the similar ionic radius of Li^+ (0.076 nm) and Ni^{2+} (0.069 nm) obstructs the extraction/insertion of Li^+ ions [6]. (2) Anisotropic strain and structural degradation from layered (space group $R\overline{3}m$) to spinel-like phase (space group $Fd\overline{3}m$) or rock-salt phase (space group $Fm\overline{3}m$) during charge/discharge processes can induce the formation of the micro-cracks along the boundaries of primary

---

[#] These authors contributed equally to this work

Corresponding author: Bin HUANG, Tel: +86-773-2538354, E-mail: bin@glut.edu.cn

DOI: 10.1016/S1003-6326(24)66468-X

particles [7]. (3) The highly oxidized Ni^{4+} ions will promptly react with the organic electrolyte at the electrode/electrolyte interface, which results in O_2 release, thermal instability and safety issues [8,9]. (4) The spontaneous reduction of Ni^{3+} to Ni^{2+}, as well as the existence of lithium residues on the surface, leads to fast moisture uptake and the formation of $LiOH/Li_2CO_3$ on the surface, consequently resulting in deteriorated performance and the gelation of cathode slurry during the electrode processing [10,11].

Many strategies have been proposed to address the aforementioned issues, such as lattice doping [12−14], surface modification [15−17] and morphology regulation [18−20]. The cation doping strategy is more facile in industry and able to enhance the cycling stability through stabilizing the crystal structure and facilitating the ions/electron diffusion. Moreover, the morphology engineering and grain orientation through the cation doping in precursors can affect the ion diffusion kinetics and structural stability [21−24]. Studies have been carried out on the morphology and structure variations of cathode materials by the introduction of foreign ion [25,26]; however, the detailed mechanisms of crystal growth and particle agglomeration have not been thoroughly explored and well demonstrated.

In this work, $LiNi_{0.88}Co_{0.09}Mn_{0.03}O_2$ materials with various contents of W-doping are synthesized from W-doped $Ni_{0.88}Co_{0.9}Mn_{0.3}(OH)_2$ precursors. Furthermore, the precursor growth mechanism in the co-precipitation process is studied.

2 Experimental

2.1 Material preparation

The spherical W-doped $Ni_{0.88}Co_{0.09}Mn_{0.03}(OH)_2$ precursors were synthesized by a co-precipitation method. The mixed salt solution with a total metal concentration of 2 mol/L was prepared by dissolving $NiSO_4\cdot 6H_2O$, $CoSO_4\cdot 7H_2O$ and $MnSO_4\cdot H_2O$ in distilled water with a molar ratio of Ni:Co:Mn=0.88:0.09:0.03. The as-prepared solution was pumped into a batch reactor (30 L) at a steady temperature (60 °C) in N_2 atmosphere. Simultaneously, $NH_3\cdot H_2O$ solution (20 wt.%) and NaOH solution (32 wt.%) were parallelly pumped into the reactor. The ammonia concentration should be maintained at 6−9 g/L and the pH value was stabilized at 11.0−11.5. The precursor powder was finally obtained after washing, filtering and vacuum drying at 140 °C for 24 h. For preparing W-doped precursors, 0.25 mol/L Na_2WO_4 solution was pumped into the reactor parallelly during the co-precipitation process without other changes. To prepare the precursors with 0.2, 0.4 and 0.6 wt.% of W dopant, the mass ratios of W to [Ni+Co+Mn] were 0.2, 0.4 and 0.6 wt.%, respectively. Accordingly, for convenience, the obtained W-doped precursors were denoted as NCMOH, NCMOH-0.2W, NCMOH-0.4W and NCMOH-0.6W, respectively. Then, W-doped $Ni_{0.88}Co_{0.09}Mn_{0.03}(OH)_2$ precursors were mixed with $LiOH\cdot H_2O$ (Li:[Ni+Co+Mn]= 1.06:1, molar ratio) and calcined at 760 °C for 12 h under a pure O_2 flow to produce W-doped cathode materials. The final products were denoted as NCM, NCM-0.2W, NCM-0.4W and NCM-0.6W, respectively.

2.2 Material characterization

The chemical compositions of the as-prepared cathode materials were determined by inductively coupled plasma-optical emission spectrometry (ICP−OES, OPTIMA 8300, PerkinElmer). The crystallographic structures of the samples were identified by powder X-ray diffraction (Rigaku, Rint−2000, Cu K_α radiation) in the 2θ range from 10° to 80°. The morphologies of the cathode particles were examined by scanning electron microscopy (SEM, FEI Quanta 250 FEG) and transmission electron microscopy (TEM, JEOL 2010). Energy dispersive X-ray spectroscopy (EDX) mapping was used for the surface elemental characterization on the W-doped precursor particles. The valences of the elements in the materials were determined using X-ray photoelectron spectroscopy (XPS, PerkinElmer, PHI 5600).

2.3 Electrochemical evaluation

Electrochemical performances were measured on CR2032 half-cells. Each working electrode was composed of 90 wt.% cathode material, 5 wt.% carbon black and 5 wt.% poly(vinylidene fluoride) (PVDF). Electrochemical tests were carried out by using an automatic galvanostatic charge/discharge system (LAND CT2001A battery tester) between 3.0 and 4.3 V (versus Li^+/Li). Electrochemical impedance spectroscopy (EIS) tests were recorded with the amplitude voltage of 5 mV in the frequency range from 10 mHz to 100 kHz on an electrochemical workstation (CHI760E).

3 Results and discussion

3.1 Physiochemical characteristics

Comparative analysis of the crystallographic structures of the precursors is displayed in Fig. S1 in Supplementary Information (SI). The samples with different amounts of W-doping have the same diffraction peaks without the presence of other impurity peaks, which can be assigned to β-Ni(OH)$_2$ (JCPDS card No. 14-0117) with a hexagonal structure [21]. The estimated intensity ratio of (001)/(101) peaks is decreased with the increase of W-doped contents, demonstrating that the crystal growth along the direction perpendicular to *c*-axis is suppressed by W-doping. The possible growth mechanism of the precursor grains is shown in Fig. 1(a). The metal ions combine with the hydroxyl groups to generate initial nucleus, which can coalesce spontaneously to form embryonic agglomerates because of the large surface energy [27]. The (001) planes have the highest concentration of hydroxyl groups, and therefore have the highest surface energy and electronegativity [23]. The electronegative (001) planes are readily adsorbed by dissociative ammonia. It has been demonstrated that the adsorbed ammonia on the (001) planes cause lowered growth rate along [001], consequently leading to (001) plane-dominated sheet-like grains [21]. When tungstate ions are added into the co-precipitation reaction,

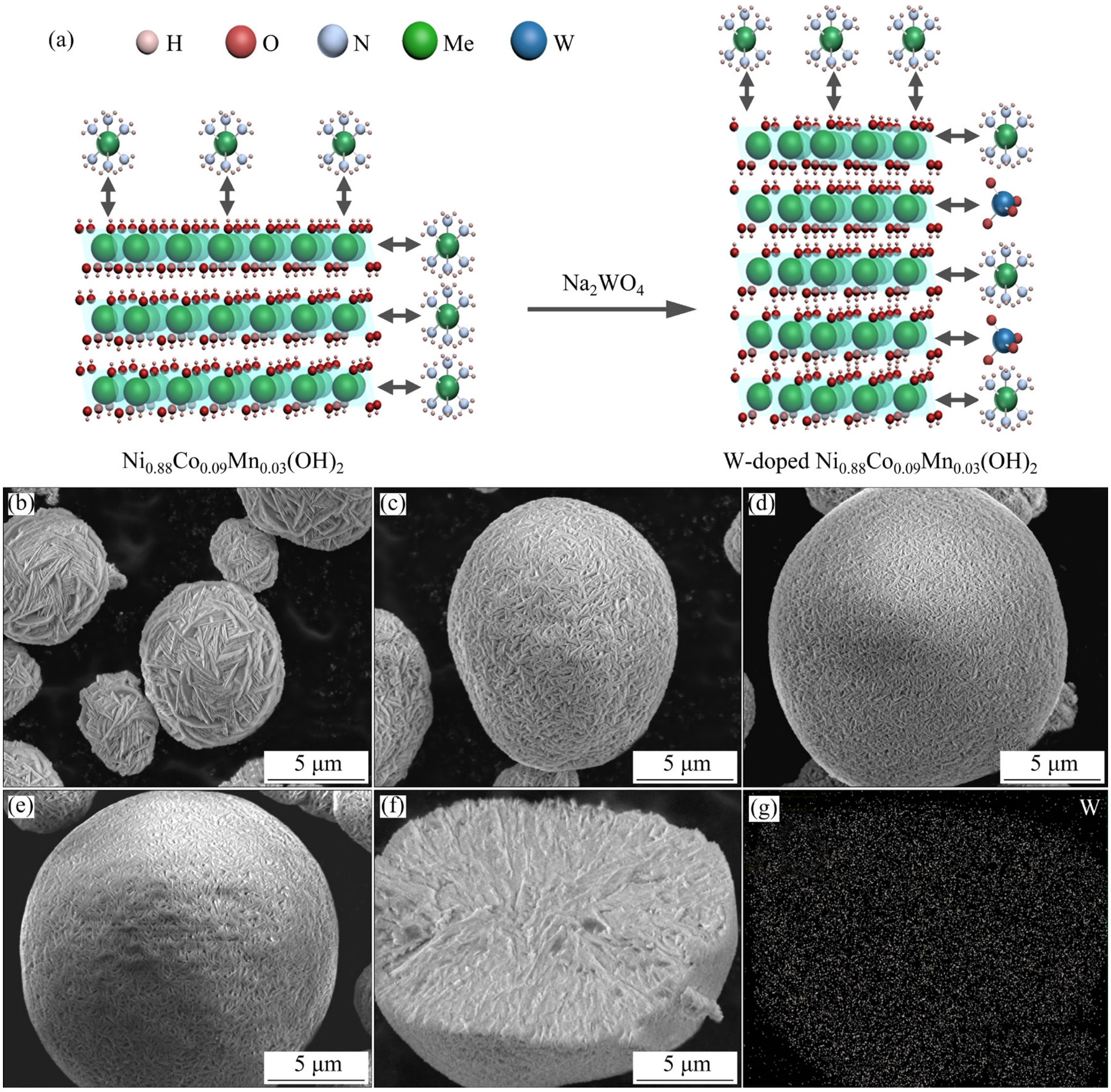

Fig. 1 Schematic illustration of effect of sodium tungstate on growth behavior of $Ni_{0.88}Co_{0.09}Mn_{0.03}(OH)_2$ (a); SEM images of NCMOH (b), NCMOH-0.2W (c), NCMOH-0.4W (d) and NCMOH-0.6W (e); EDX elemental mapping of NCMOH-0.4W (f, g)

things will change. Since $MeWO_4$ (Me^{2+}=Ni^{2+}, Co^{2+} or Mn^{2+}) possesses lower dissociation constant than $Me(OH)_2$, Me^{2+} ions are easier to combine with WO_4^{2-} than OH^- ions. As a result, the selective adsorption of WO_4^{2-} would preferentially occur on (101) planes, which have less hydroxyl groups and thus provide more accessible Me^{2+} cation sites. Therefore, the crystal growth along [001] direction can be promoted. This is the reason why W-doped precursors exhibit lower intensity ratio of (001)/(101) peaks.

The morphology evolution of the precursors is analyzed by SEM, as shown in Figs. 1(b−e), which reveals the relationship between the particle morphology and doping amount. All particles show a spherical morphology with a diameter of ~10 μm, and are composed of nanoscale primary particles. With the increase of W-doping, both the length and width of the primary particles show obvious shrinkage and their morphology changes from lamellar grains to spindle-like shape. The finer grain size of the W-doped samples is due to the pinning effect of W on grain boundaries, which inhibits grain growth. Figures 1(f) and S2 in SI display the elemental mapping results of NCMOH-0.4W. The homogeneous distribution of Ni, Co, Mn and W elements further indicates that WO_4^{2-} has been uniformly incorporated into the precursor by co-precipitation method.

The contents of W in the as-prepared cathode materials were measured by ICP−OES. The results (Table S1 in SI) confirm that the content of W in each sample is very close to the designed value. Figure 2 shows the XRD patterns of the cathode materials with different amounts of W-doping. All the patterns can be indexed as α-$NaFeO_2$ layered structure (JCPDS card No. 09-0063) with $R\overline{3}m$ space group without any impurity peak. The similar XRD results demonstrate that the W-doping has little influence on the crystallographic structure (Fig. 2(a)). Meanwhile, it can be observed that the (006)/(102) and (008)/(110) diffraction peaks have obvious splitting, suggesting a well-ordered layered structure formed in all samples (Fig. 2(b)).

The detailed lattice parameters can be obtained by using the Rietveld refinement, as shown in Figs. 2(c−f) and Table 1. The calculated patterns are highly coincident with the obtained data, and the low values of residual of least-squares refinement (R_{wp}) and weighted residual of least-squares refinement (R_p) (less than 5%) demonstrate that our refined results are credible. As can be seen in Table 1, with increase of the doping amount of W, the degree of Li^+/Ni^{2+} mixing is enhanced, in agreement with the decrease of (003)/(104) peak intensity ratio [28]. According to the charge balance principle, the introduction of W^{6+} will generate more Ni^{2+}, which results in the increased cation mixing due to the similar ionic radii of Li^+ and Ni^{2+}, confirming that the W^{6+} has exclusively occupied the transition-metal sites. In addition, Ni^{2+} has the larger ionic radius than Ni^{3+}, which will extend the cell volume of materials [14]. As expected, the cell volume calculated by utilizing refined lattice parameters is enlarged due to the presence of W. It should be mentioned that the increased cation mixing originating from the W-doping is unlike that caused by the unsuitable calcination condition (e.g., insufficient oxygen supply) for synthesis of the cathode. The former is mainly present in the near-surface region of the primary particles and is an ordered occupation of Li sites by Ni^{2+} ions, which is considered to be able to protect the cathode surface and improve cycling stability [29].

The morphologies of all the products are shown in Fig. 3. The pristine and W-doped samples exhibit a spherical morphology with an average diameter of ~10 μm. The size distributions of the samples are listed in Table S2 in SI. The spherical secondary particles are composed of nanosized primary particles; however, the W-doped samples show smaller primary particles than the pristine one, which is consistent with the phenomenon observed on the precursors. Figures 3(c, f) show the cross-sectional SEM images of the NCM and NCM-0.4W, respectively. It can be clearly seen that the primary particles of the former are much larger than that of the latter. In addition, the pristine NCM is composed of randomly orientated equiaxed grains, whereas the W-doped sample has slender and narrow grains with a radial growth pattern. The unique structure derived from the W-doping is beneficial for Li^+ diffusion, and can alleviate the anisotropic strain during charge−discharge process [30]. TEM and high-resolution TEM (HRTEM) images of NCM are shown in Figs. 3(g, h). The spacing of the lattice fringes is 0.47 nm (Fig. 3(h)), which can be assigned to the (003) crystal planes. The lattice fringe spacing of NCM-0.4W is 0.48 nm (Fig. 3(j)), suggesting that W-doping might broaden the diffusion paths for Li^+ ions.

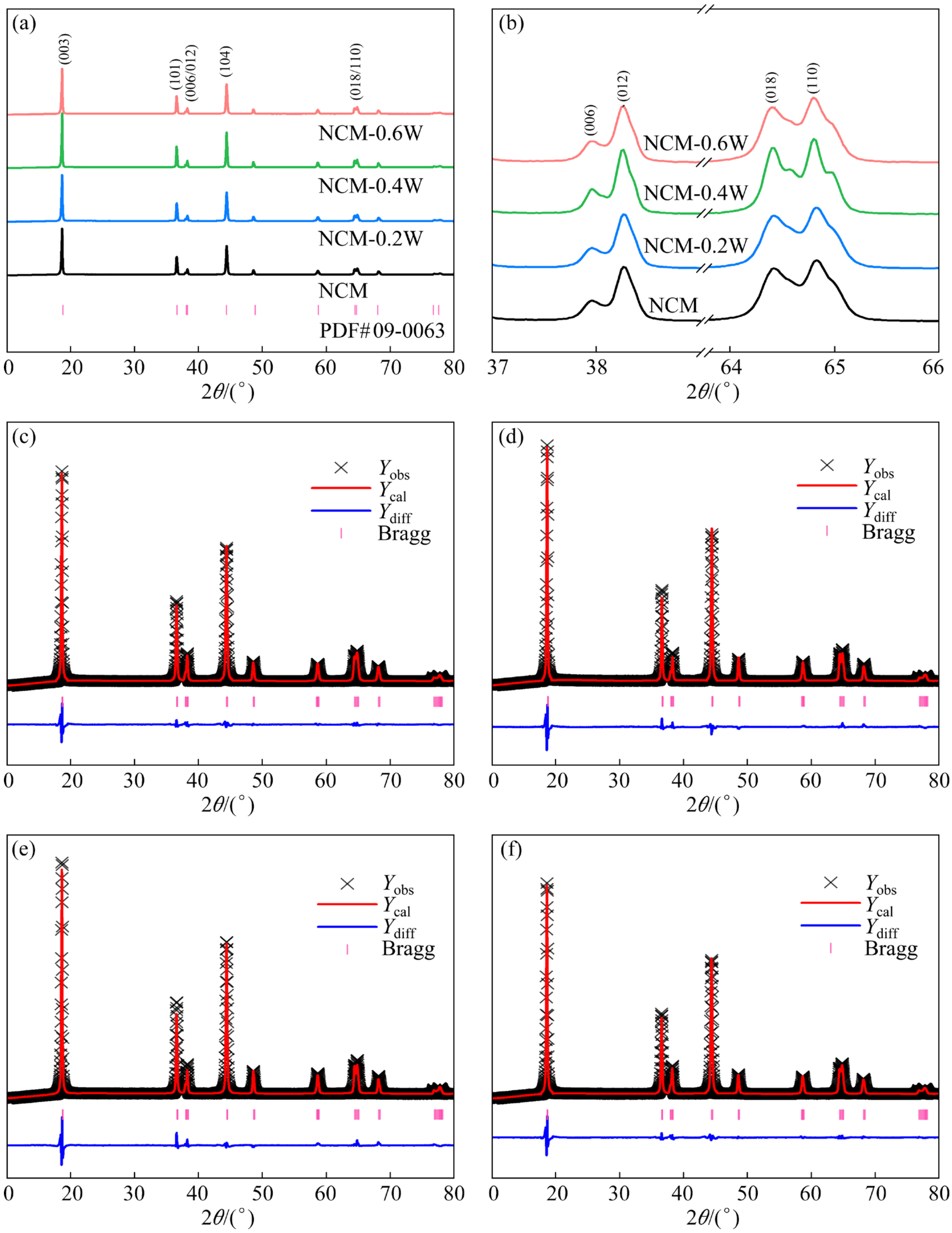

Fig. 2 XRD patterns of NCM and W-modified cathode materials (a); enlarged regions for (006/012), (018/110) peaks (b); Rietveld refinements of NCM (c), NCM-0.2W (d), NCM-0.4W (e) and NCM-0.6W (f)

Table 1 Rietveld analysis results of NCM and W-modified cathode materials

Sample	a/Å	c/Å	$I_{(003)}/I_{(104)}$	Ni/Li mixing/%	R_{wp}/%	R_p/%
NCM	2.8722	14.1953	1.6077	0.78	3.38	1.87
NCM-0.2W	2.8762	14.1898	1.5601	0.92	3.7	1.5
NCM-0.4W	2.8725	14.1918	1.5291	1.4	3.41	1.72
NCM-0.6W	2.8745	14.2024	1.5223	1.95	2.8	1.44

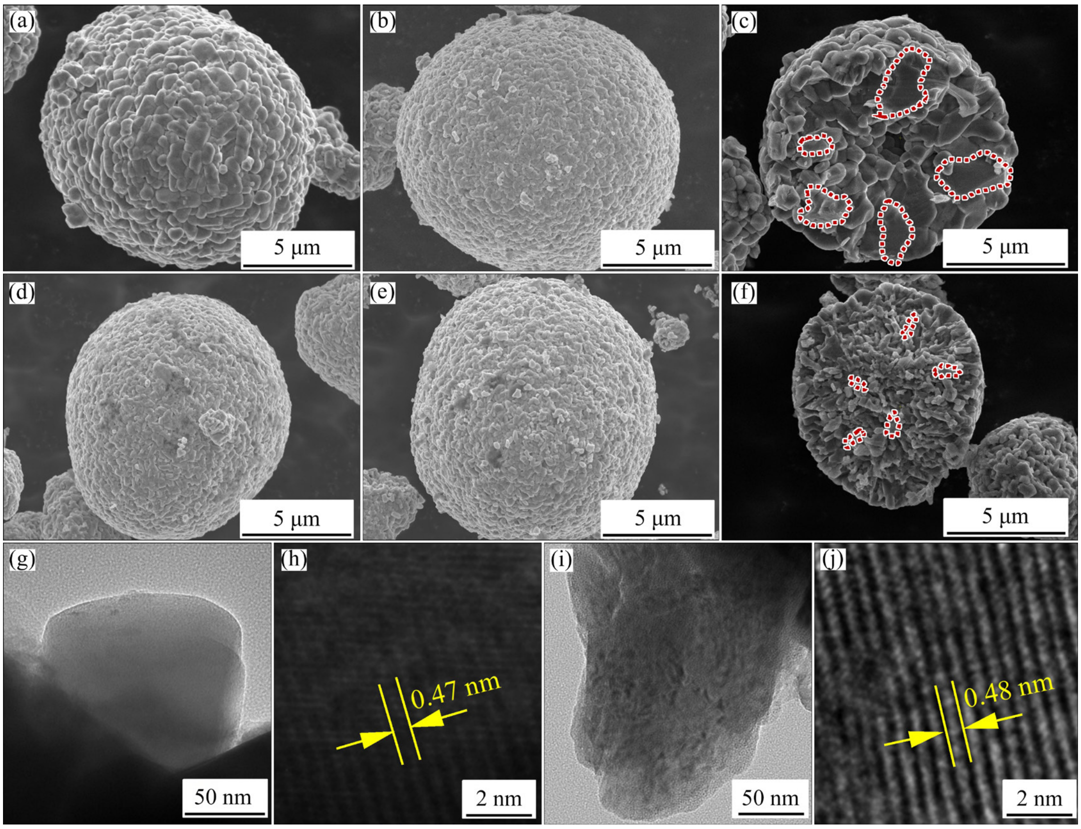

Fig. 3 SEM images of NCM (a), NCM-0.2W (b), NCM-0.4W (d) and NCM-0.6W (e); cross-sectional images of NCM (c) and NCM-0.4W (f); TEM and HR-TEM images of NCM (g, h) and NCM-0.4W (i, j)

Figure 4 shows the XPS results of the NCM and the NCM-0.4W samples. The Ni spectra with two main peaks at 854.7 and 872.3 eV are assigned to Ni $2p_{3/2}$ and Ni $2p_{1/2}$, respectively (Fig. 4(a)). The peak of Ni $2p_{3/2}$ can be deconvoluted into two peaks at 855.63 and 854.5 eV, which belong to Ni^{3+} and Ni^{2+}, respectively, indicating that Ni^{3+} and Ni^{2+} coexist in the materials. The $Ni^{2+}/(Ni^{2+}+Ni^{3+})$ values can be calculated to predict the degree of cation mixing. These values of NCM and NCM-0.4W are 19.25% and 31.2%, respectively, which means that W-doping increases the cation mixing. This result is consistent with the XRD Rietveld refinement results. The high-resolution Co 2p XPS spectrum (Fig. 4(b)) exhibits two main peaks located at 779.6 and 794.73 eV, which represent Co $2p_{3/2}$ and Co $2p_{1/2}$, respectively, indicating the presence of Co^{3+}. As can be seen in the Mn 2p spectrum (Fig. 4(c)), two broad diffraction peaks are observed at 642.09 and 653.41 eV, corresponding to Mn $2p_{3/2}$ and Mn $2p_{1/2}$, respectively, indicating that the valence state of Mn is +4. The spectrum of W 4f (Fig. 4(d)) shows two spin orbital peaks at 34.69 and 36.84 eV, which are assigned to W $4f_{7/2}$ and W $4f_{5/2}$, respectively, indicating that the valence state of W is +6 [31].

3.2 Electrochemical properties

Electrochemical performances of the as-prepared cathode materials were evaluated in CR2032 coin type half-cells in the operating voltage range of 3−4.3 V at room temperature and elevated temperature. As shown in Fig. 5(a), all the samples show very similar charge and discharge curves. When tested at 25 °C, NCM-0.2W, NCM-0.4W and NCM-0.6W display initial discharge capacities of 192, 190.3 and 188.9 mA·h/g, respectively, while the pristine NCM delivers the value of 202.8 mA·h/g. The lowered capacity caused by W-doping can be interpreted as the electrochemical inactivity of W dopant in the cathodes. When tested at 45 °C, the initial capacities of the samples are increased due to the enhanced ion diffusion kinetics at high temperature (Fig. 5(d)). However, the pristine NCM exhibits inferior cycling performance to the W-doped ones, both at room temperature and 45 °C (Figs. 5(c, f)). Moreover, the comparison of cycling performance

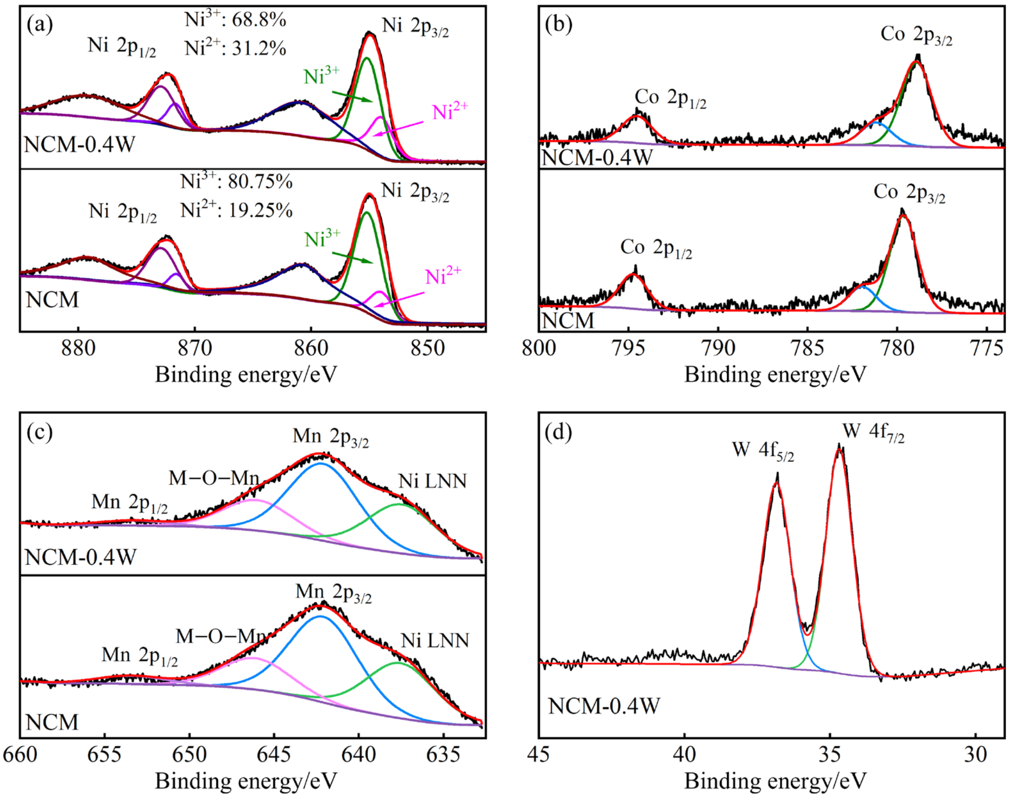

Fig. 4 XPS spectra and fitting results of NCM and NCM-0.4W cathode materials: (a) Ni 2p; (b) Co 2p; (c) Mn 2p; (d) W 4f

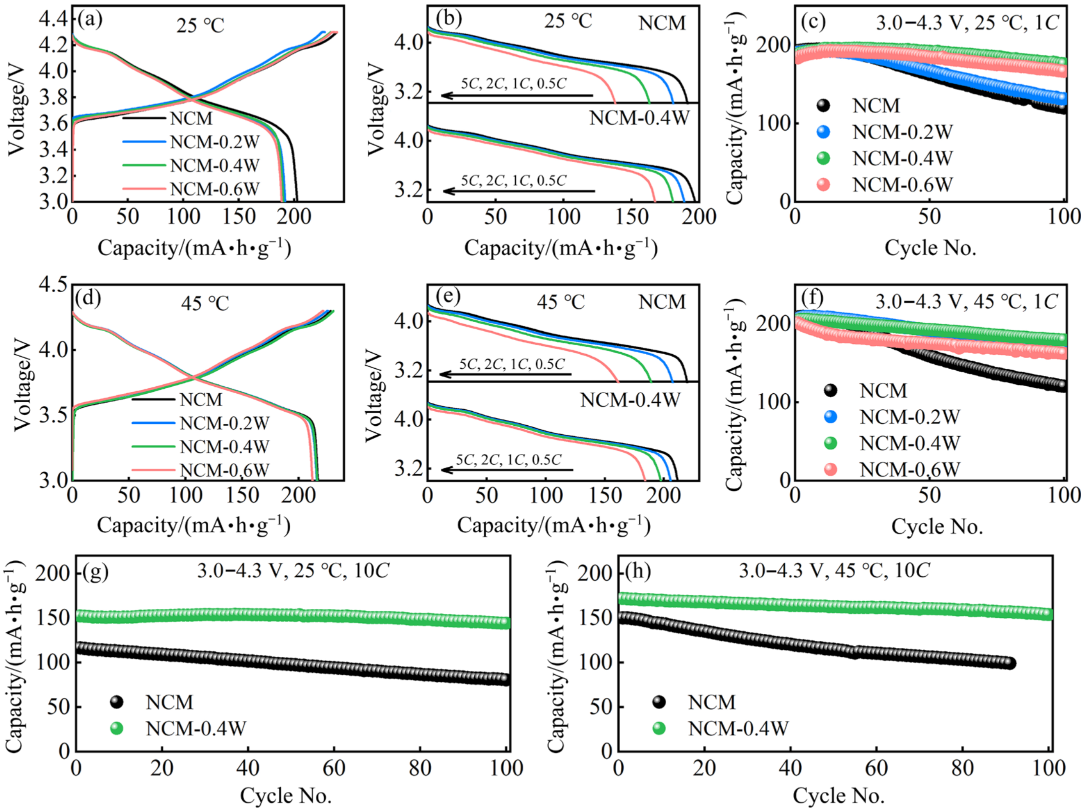

Fig. 5 Initial charge−discharge curves at 0.1C (1C=200 mA/g) at 25 °C (a) and 45 °C (d); Discharge curves at 0.5C, 1C, 2C and 5C at 25 °C (b) and 45 °C (e); Cycling performances at 1C at 25 °C (c) and 45 °C (f); Cycling performances of NCM and NCM-0.4W at 10C at 25 °C (g) and 45 °C (h)

among these samples indicates that NCM-0.4W possesses not only excellent cycling stability, but also the highest specific capacity. When tested at 25 °C, for example, it delivers a specific capacity of 175.8 mA·h/g at 1*C* after 100 cycles with the capacity retention of 93.51%, which is higher than the values of NCM (119.7 mA·h/g, 62.21%), NCM-0.2W (131.5 mA·h/g, 69.03%) and NCM-0.6W (166.7 mA·h/g, 90.59%). Hence, NCM-0.4W is chosen as a typical sample to illustrate the merits of W-doping.

Rate capability is compared between NCM and NCM-0.4W, as shown in Figs. 5(b, e). Both samples show capacity fading as the current density increases. However, it can be seen that the fading rate of NCM-0.4W is significantly suppressed, suggesting the better Li^+ diffusion kinetics endowed by W-doping. Comparison of cycling performances at higher current density can magnify the difference between their Li^+ diffusion kinetics. Figures 5(g, h) display the cycling performances of NCM and NCM-0.4W at 10*C*. When tested at 25 °C, the W-doped sample still achieves a capacity of 144.2 mA·h/g after 100 cycles with a retention of 94.68%. In contrast, the pristine NCM rapidly fades to 80.7 mA·h/g after 100 cycles at 10*C*. Similar trends are also observed at the testing temperature of 45 °C.

In order to further understand the phase transitions accompanying with charge/discharge cycling, d*Q*/d*V*−*V* profiles are depicted for NCM and NCM-0.4W cathodes in Fig. 6. The d*Q*/d*V*−*V* curves of NCM and NCM-0.4W contain three couples of peaks. The three oxidation peaks for both samples are related to the oxidation of Ni^{3+} (with minor Ni^{2+}) to Ni^{4+}, and Co^{3+} to Co^{4+}, accompanied with the transitions from hexagonal phase to monoclinic phase (H1/M), monoclinic phase to hexagonal phase (M/H2) and hexagonal phase to hexagonal phase (H2/H3). The three reduction peaks for both samples are indicative of the reverse process [32−35]. The reversibility of H2-H3 phase transition at about 4.2 V is closely related to the cycling stability [17,35]. Obviously, the H2/H3 peak of the NCM sample fades dramatically after 100 cycles, indicating the inferior structural stability (Fig. 6(a)). In contrast, H2/H3 peak of NCM-0.4W remains unchanged in 50 cycles, and changes slightly up to 100 cycles, indicating improved structural stability (Fig. 6(b)).

To evaluate the reaction kinetics degradation, electrochemical impedance spectroscopy (EIS) after 100 cycles has been implemented. As can be seen in Fig. 7(a), both plots consist of two partly merged

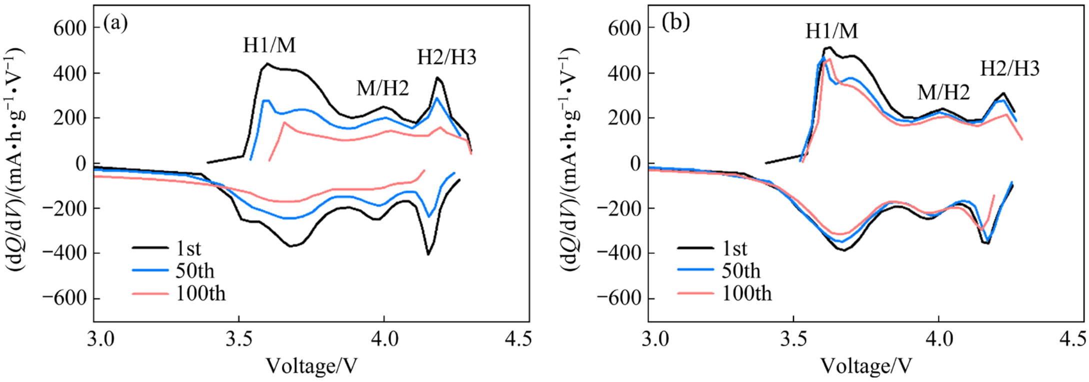

Fig. 6 d*Q*/d*V*−*V* curves of NCM (a) and NCM-0.4W (b)

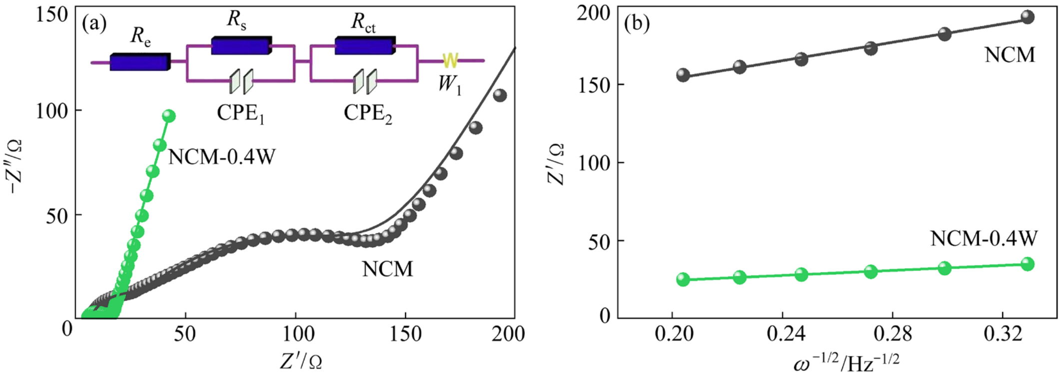

Fig. 7 Nyquist curves of NCM and NCM-0.4W (a) and corresponding Z'−$\omega^{-1/2}$ plots (ω is the frequency) (b)

semicircles at high-to-medium frequency region and a straight line at low frequency region, corresponding to surface resistance (R_s), charge transfer resistance (R_{ct}) at the electrolyte/electrode interface and Warburg impedance connected with Li^+ diffusion in solid electrode, respectively [36]. The diffusion coefficient of Li^+ (D_{Li}^{+}) is also calculated, according to Eq. (1). The parameter σ can be obtained from the slop of $Z'-\omega^{-1/2}$ plot (Fig. 7(b)), according to Eq. (2) [37,38]:

$$D_{Li}^{+}=R^2T^2/(2A^2n^4F^4C^2\sigma^2) \tag{1}$$

$$Z'=R_e+R_{ct}+\sigma\omega^{-1/2} \tag{2}$$

where R is the molar gas constant, T represents the thermodynamic temperature, A is the active surface area, n stands for the transfer electron numbers during the reaction, F stands for the Faraday constant, C represents the concentration of lithium ions, σ is the Warburg factor. The results are shown in Table 2. According to the calculation results, after 100 cycles, the diffusion coefficient of Li^+ for NCM-0.4W is 1.617×10^{-15} cm^2/s, which is much larger than that of NCM (1.200×10^{-16} cm^2/s), indicating that the W-doping has a positive effect on Li^+ diffusion kinetics.

Table 2 EIS fitting parameters and diffusion coefficients of Li^+ for NCM and NCM-0.4W samples

Sample	$(R_s+R_{ct})/\Omega$	σ	$D_{Li}^{+}/(cm^2\cdot s^{-1})$
NCM	268.68	293.38	1.200×10^{-16}
NCM-0.4W	14.232	79.903	1.617×10^{-15}

3.3 Evolution of morphology and structure after cycles

Figure 8 displays SEM images and XRD patterns of NCM and NCM-0.4W cathodes after 100 cycles. After repetitive de-lithiation/lithiation

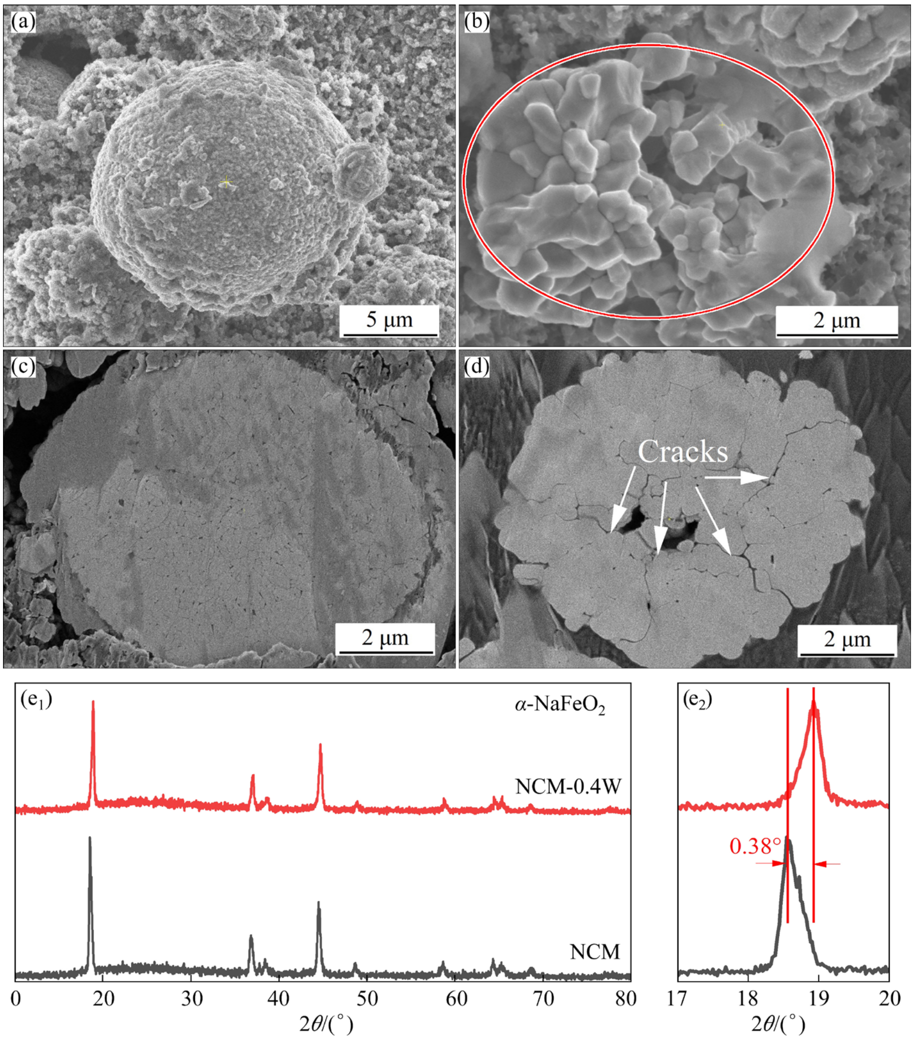

Fig. 8 SEM images (a, b) and cross-sectional images (c, d) of NCM-0.4W (a, c) and NCM (b, d) after 100 cycles and XRD patterns (e) after 100 cycles

processes, some NCM particles are shattered into fragments (Fig. 8(b)), and numerous intergranular microcracks are observed (Fig. 8(d)). The microcracks result from volume contraction and expansion during cycling, which not only let electrolyte penetrate into the particles to initiate extra side-reactions, but also restrain the migration of Li^+ ions. The morphology of NCM-0.4W samples is well maintained without obvious microcracks formed after cycling (Figs. 8(a, c)). Furthermore, as shown in Fig. 8(e), the diffraction peak of (003) facets for NCM shift towards lower angle with 0.38° compared with that for NCM-0.4W, indicating a larger lattice expansion. However, this shift is unlike the situation that an expanded interplanar spacing can promote diffusion kinetics for Li ions. This is caused by the lattice expansion along *c*-axis with the deepening of delithiation. In a highly delithiated NCM cathode, the metastable Ni^{4+} ions are readily reduced into more stable Ni^{2+} ions and thus the electrochemically inactive rock salt NiO phase is formed [39]. In this case, the lattice variation cannot be fully restored after re-lithiation. Therefore, the results prove that W-doping can stabilize the material structure and suppress the formation of microcracks during cycling.

4 Conclusions

(1) W-doped Ni-rich cathode materials with ordered primary particles were successfully synthesized from W-doped hydroxide precursors which were obtained by co-precipitation method with the presence of sodium tungstate.

(2) The crystal growth of the precursor can be influenced by the selective adsorption of WO_4^{2-}. W-doping leads to smaller primary particles with radial orientation.

(3) The sample with 0.4 wt.% W-doping exhibits the best electrochemical properties. At room temperature, it delivers an initial discharge capacity of 190.3 mA·h/g at 0.1*C*, and a capacity retention of 94.68% after 100 cycles at a high rate of 10*C*. It also shows excellent cycling stability at 45 °C.

(4) The intergranular cracks, as well as the lattice variation after 100 cycles can be suppressed by W-doping, indicating that W-doping can improve the structural stability for Ni-rich layered cathodes.

CRediT authorship contribution statement

Lei CHENG: Conceptualization, Formal analysis, Writing − Original draft; **Yi ZHAO:** Methodology, Investigation; **Bin HUANG:** Supervision, Project administration, Resources, Funding acquisition, Writing − Review & editing, Investigation; **Zao-wen ZHAO:** Validation; **Yan-wei LI:** Data curation, Software; **Wei LI:** Funding acquisition.

Declaration of competing interest

The authors declare that they have no known competing financial interests or personal relationships that could have appeared to influence the work reported in this paper.

Acknowledgments

This work was supported by the National Natural Science Foundation of China (No. 52004076), the Science and Technology Base and Talent Project of Guangxi, China (No. GUIKEAD20159049) and the Guangxi Natural Science Foundation, China (No. 2020GXNSFAA297054).

Supplementary Information

Supplementary Information in this paper can be found at: http://tnmsc.csu.edu.cn/download/16-p1251-2022-1146-Supplementary_Information.pdf.

References

[1] LIU Si-yu, ZHOU Yu-huan, ZHANG Yi-bin, XIA Sheng-jie, LI Ying, ZHOU Xin, QIU Bao, SHAO Guang-jie, LIU Zhao-ping. Surface yttrium-doping induced by element segregation to suppress oxygen release in Li-rich layered oxide cathodes [J]. Tungsten, 2022, 4(4): 336−345.

[2] ZHANG Bao, LI Ling-jun, ZHENG Jun-chao. Characterization of multiple metals (Cr, Mg) substituted $LiNi_{0.8}Co_{0.1}Mn_{0.1}O_2$ cathode materials for lithium ion battery [J]. Journal of Alloys and Compounds, 2012, 520: 190−194.

[3] LIU Wen, OH P, LIU Xi-en, LEE M J, CHO W, CHAE S, KIM Y, CHO J. Nickel-rich layered lithium transition-metal oxide for high-energy lithium-ion batteries [J]. Angewandte Chemie International Edition, 2015, 54: 4440−4457.

[4] LI Wen-bin, WU Kang, FENG Hao, WANG Ni, ZHANG Jiang-hua, WANG Jing-jing, LI Xi-fei. Atomic layer deposition of ultrafine Pd nanoparticles for enhancing the rate capability of $LiNi_{0.8}Co_{0.1}Mn_{0.1}O_2$ cathode [J]. Tungsten, 2022, 4(4): 346−355.

[5] CHO E, SEO S W, MIN K. Theoretical prediction of surface stability and morphology of $LiNiO_2$ cathode for Li ion batteries [J]. ACS Applied Materials & Interfaces, 2017, 9: 33257−33266.

[6] WANG Jia-le, LIU Cheng-jin, XU Guan-li, MIAO Chang, WEN Min-yue, XU Ming-biao, WANG Chang-jun, XIAO Wei. Strengthened the structural stability of in-situ F^- doping

Ni-rich $LiNi_{0.8}Co_{0.15}Al_{0.05}O_2$ cathode materials for lithium-ion batteries [J]. Chemical Engineering Journal, 2022, 438: 135537.

[7] XIN Feng-xia, ZHOU Hui, CHEN Xiao-bo, ZUBA M, CHERNOVA N, ZHOU Guang-wen, WHITTINGHAM M S. Li−Nb−O coating/substitution enhances the electrochemical performance of $LiNi_{0.8}Mn_{0.1}Co_{0.1}O_2$ (NMC 811) cathode [J]. ACS Applied Materials & Interfaces, 2019, 11: 34889−34894.

[8] YOON C S, PARK K J, KIM U H, KANG K H, RYU H H, SUN Y K. High-energy Ni-rich $Li[Ni_xCo_yMn_{1-x-y}]O_2$ cathodes via compositional partitioning for next-generation electric vehicles [J]. Chemistry of Materials, 2017, 29: 10436−10445.

[9] LI Yong-chun, XIANG Wei, WU Zhen-guo, XU Chun-liu, XU Ya-di, XIAO Yao, YANG Zu-guang, WU Chun-jin, LV Gen-pin, GUO Xiao-dong. Construction of homogeneously Al^{3+} doped Ni rich Ni−Co−Mn cathode with high stable cycling performance and storage stability via scalable continuous precipitation [J]. Electrochimica Acta, 2018, 291: 84−94.

[10] HATSUKADE T, SCHIELE A, HARTMANN P, BREZESINSKI T, JANEK J. Origin of carbon dioxide evolved during cycling of nickel-rich layered NCM cathodes [J]. ACS Applied Materials & Interfaces, 2018, 10: 38892−38899.

[11] KIM J, LEE J, MA H, JEONG H Y, CHA H, LEE H, YOO Y, PARK M, CHO J. Controllable solid electrolyte interphase in nickel-rich cathodes by an electrochemical rearrangement for stable lithium-ion batteries [J]. Advanced Materials, 2018, 30: 1704309.

[12] WEIGEL T, SCHIPPER F, ERICKSON E M, SUSAI F A, MARKOVSKY B, AURBACH D. Structural and electrochemical aspects of $LiNi_{0.8}Co_{0.1}Mn_{0.1}O_2$ cathode materials doped by various cations [J]. ACS Energy Letters, 2019, 4: 508−516.

[13] WANG Li-fan, LIU Gao-yang, DING Xian-an, ZHAN Chun, WANG Xin-dong. Simultaneous coating and doping of a Nickel-rich cathode by an oxygen ion conductor for enhanced stability and power of Lithium ion batteries [J]. ACS Applied Materials & Interfaces, 2019, 11: 33901−33912.

[14] PARK G T, RYU H H, PARK N Y, YOON C S, SUN Y K. Tungsten doping for stabilization of $Li[Ni_{0.90}Co_{0.05}Mn_{0.05}]O_2$ cathode for Li-ion battery at high voltage [J]. Journal of Power Sources, 2019, 442: 227242.

[15] LI Xin-ze, CHENG Lei, CHEN Li-ming, HUANG Bin, YANG Jian-wen, LI Yan-wei, LI Wei. Stabilizing the surface of $LiNi_{0.815}Co_{0.15}Al_{0.035}O_2$ by a facile pre-oxidation-coating strategy on the precursor [J]. Solid State Ionics, 2022, 386: 116028.

[16] DENG Si-xu, LI Xia, REN Zhou-hong, LI Wei-han, LUO Jing, LIANG Jian-wen, LIANG Jian-neng, BANIS M N, LI Min-si, ZHAO Yang, LI Xiao-na, WANG Chang-hong, SUN Yi-peng, SUN Qian, LI Ru-ying, HU Yong-feng, HUANG Huan, ZHANG Li, LU Shi-gang, LUO Jun, SUN Xue-liang. Dual-functional interfaces for highly stable Ni-rich layered cathodes in sulfide all-solid-state batteries [J]. Energy Storage Materials, 2020, 27: 117−123.

[17] XIAO Wei, NIE Yan, MIAO Chang, WANG Jia-le, TAN Yi, WEN Min-yue. Structural design of high-performance Ni-rich $LiNi_{0.83}Co_{0.11}Mn_{0.06}O_2$ cathode materials enhanced by Mg^{2+} doping and Li_3PO_4 coating for lithium ion battery [J]. Journal of Colloid and Interface Science, 2022, 607: 1071−1082.

[18] ZENG Tian-yi, ZHANG Xiao-yun, QU Xing-yu, LI Mei-qing, ZHANG Pan-pan, SU Ming-ru, DOU Ai-chun, NAVEED A, ZHOU Yu, LIU Yun-jian. Mechanism exploration of enhanced electrochemical performance of single-crystal versus polycrystalline $LiNi_{0.8}Mn_{0.1}Co_{0.1}O_2$ [J]. Rare Metals, 2022, 41: 3783−3794.

[19] CHENG Lei, ZHANG Bao, SU Shi-lin, MING Lei, ZHAO Yi, WANG Chun-hui, OU Xing. Comparison of monocrystalline and secondary $LiNi_{0.5}Co_{0.2}Mn_{0.3}O_2$ cathode material for high-performance lithium-ion batteries [J]. Journal of Alloys and Compounds, 2020, 845: 156202.

[20] QIAN Guan-nan, ZHANG You-tian, LI Lin-sen, ZHANG Rui-xin, XU Jun-meng, CHENG Zhen-jie, XIE Si-jie, WANG Han, RAO Qun-li, HE Yu-shi, SHEN Yan-bin, CHEN Li-wei, TANG Ming, MA Zi-feng. Single-crystal nickel-rich layered-oxide battery cathode materials: synthesis, electrochemistry, and intra-granular fracture [J]. Energy Storage Materials, 2020, 27: 140−149.

[21] YANG Xi, HUANG Xue-song, SHI Han-cheng, DONG Peng, WANG Ding, DUAN Jian-guo, ZHANG Ying-jie. Growth mechanisms for spherical $Ni_{0.815}Co_{0.15}Al_{0.035}(OH)_2$ precursors prepared via the ammonia complexation precipitation method [J]. Journal of Energy Chemistry, 2021, 53: 379−386.

[22] LEI Yi-ke, AI Jin-jin, YANG Shuai, JIANG Hong-yu, LAI Chun-yan, XU Qun-jie. Effect of flower-like $Ni(OH)_2$ precursors on Li^+/Ni^{2+} cation mixing and electrochemical performance of nickel-rich layered cathode [J]. Journal of Alloys and Compounds, 2019, 797: 421−431.

[23] YANG Yue, XU Sheng-ming, XIE Ming, HE Ying-he, HUANG Guo-yong, YANG You-cai. Growth mechanisms for spherical mixed hydroxide agglomerates prepared by co-precipitation method: A case of $Ni_{1/3}Co_{1/3}Mn_{1/3}(OH)_2$ [J]. Journal of Alloys and Compounds, 2015, 619: 846−853.

[24] LI Ji-li, YAO Rui-min, CAO Chuan-bao. $LiNi_{1/3}Co_{1/3}Mn_{1/3}O_2$ nanoplates with {010} active planes exposing prepared in polyol medium as a high-performance cathode for Li-ion battery [J]. ACS Applied Materials & Interfaces, 2014, 6: 5075−5082.

[25] LIANG Chao-ping, LONGO R C, KONG Fan-tai, ZHANG Chen-xi, NIE Yi-fan, ZHENG Yong-ping, CHO K. Ab initio study on surface segregation and anisotropy of Ni-rich $LiNi_{1-2y}Co_yMn_yO_2$ (NCM) ($y \le 0.1$) cathodes [J]. ACS Applied Materials & Interfaces, 2018, 10: 6673−6680.

[26] GARCIA J C, BAREñO J, YAN Jian-hua, CHEN Guo-ying, HAUSER A, CROY J R, IDDIR H. Surface structure, morphology, and stability of $Li(Ni_{1/3}Mn_{1/3}Co_{1/3})O_2$ cathode material [J]. The Journal of Physical Chemistry C, 2017, 121: 8290−8299.

[27] HUANG Bin, CHENG Lei, LI Xin-ze, ZHAO Zao-wen, YANG Jian-wen, LI Yan-wei, PANG You-yong, CAO Guo-zhong. Layered cathode materials: Precursors, synthesis, microstructure, electrochemical properties, and battery performance [J]. Small, 2022, 18: 2107697.

[28] WANG Chun-hui, SHAO Li, GUO Xin, XI Xiao-ming,

YANG Li-shan, HUANG Cheng-huan, ZHOU Chun-xian, ZHAO Hai-hong, YIN Du-lin, WANG Zhong-chang. Air-induced degradation and electrochemical regeneration for the performance of layered Ni-rich cathodes [J]. ACS Applied Materials & Interfaces, 2019, 11: 44036−44045.

[29] RYU H H, PARK G T, YOON C S, SUN Y K. Suppressing detrimental phase transitions via tungsten doping of $LiNiO_2$ cathode for next-generation lithium-ion batteries [J]. Journal of Materials Chemistry A, 2019, 7: 18580−18588.

[30] YANG Cheng-kai, QI Li-ya, ZUO Zi-cheng, WANG Ru-na, YE Meng, LU Jing, ZHOU Heng-hui. Insights into the inner structure of high-nickel agglomerate as high-performance lithium-ion cathodes [J]. Journal of Power Sources, 2016, 331: 487−494.

[31] CHUKWUIKE V I, SANKAR S S, KUNDU S, BARIK R C. Capped and uncapped nickel tungstate ($NiWO_4$) nanomaterials: A comparison study for anti-corrosion of copper metal in NaCl solution [J]. Corrosion Science, 2019, 158: 108101.

[32] LU Shi-jie, LIU Yang, HE Zhen-jiang, LI Yun-jiao, ZHENG Jun-chao, MAO Jing, DAI Ke-hua. Synthesis and properties of single-crystal Ni-rich cathode materials in Li-ion batteries [J]. Transactions of Nonferrous Metals Society of China, 2021, 31: 1074−1086.

[33] TAI Zi-ge, LI Xing-long, ZHU Wei, SHI Ming, XIN Yan-fei, GUO Sheng-wu, WU Yi-fang, CHEN Yuan-zhen, LIU Yong-ning. Nonstoichiometry of Li-rich cathode material with improved cycling ability for lithium-ion batteries [J]. Journal of Colloid and Interface Science, 2020, 570: 264−272.

[34] ZHU Wei, TAI Zi-ge, SHU Cheng-yong, CHONG Shao-kun, GUO Sheng-wu, JI Li-jie, CHEN Yuan-zhen, LIU Yong-ning. The superior electrochemical performance of a Li-rich layered cathode material with Li-rich spinel $Li_4Mn_5O_{12}$ and MgF_2 double surface modifications [J]. Journal of Materials Chemistry A, 2020, 8: 7991−8001.

[35] CAO Yuan-lin, YANG Xiu-kang, WANG Lu, XIAO Ling, FU Ni, ZOU Li, MA Wen-bo, LIU Zhe-ting, WANG Xiao-qin, LIU Li, SHU Hong-bo, WANG Xian-you. Improving electrochemical performance of Ni-rich layered oxide cathodes via one-step dual modification strategy [J]. Transactions of Nonferrous Metals Society of China, 2022, 32: 3663−3678.

[36] LI Fang-cheng, ZHANG Gang, ZHANG Zong-liang, YANG Jian, LIU Fang-yang, JIA Ming, JIANG Liang-xing. Regeneration of Al-doped $LiNi_{0.5}Co_{0.2}Mn_{0.3}O_2$ cathode material by simulated hydrometallurgy leachate of spent lithium-ion batteries [J]. Transactions of Nonferrous Metals Society of China, 2022, 32: 593−603.

[37] WANG Ruo-xing, LI Zhi-min, YANG Zi, ZHANG Mao-lin, ZHANG Dong-yan, YAN Yang-xi. Synergistic effect of Ce^{4+} modification on the electrochemical performance of $LiNi_{0.6}Co_{0.2}Mn_{0.2}O_2$ cathode materials at high cut-off voltage [J]. Ceramics International, 2021, 47: 1268−1276.

[38] WANG Chun-hui, ZHANG Bao, XIA Hai-feng, CAO Liang, LUO Bi, FAN Xin-ming, ZHANG Jia-feng, OU Xing. Composition and architecture design of double-shelled $Co_{0.85}Se_{1-x}S_x$@carbon/graphene hollow polyhedron with superior alkali (Li, Na, K)-ion storage [J]. Small, 2020, 16: e1905853.

[39] WU Feng, LIU Na, CHEN Lai, SU Yue-feng, TAN Guo-qiang, BAO Li-ying, ZHANG Qi-yu, LU Yun, WANG Jing, CHEN Shi, TAN Jing. Improving the reversibility of the H2-H3 phase transitions for layered Ni-rich oxide cathode towards retarded structural transition and enhanced cycle stability [J]. Nano Energy, 2019, 59: 50−57.

钨掺杂对 $LiNi_{0.88}Co_{0.09}Mn_{0.03}O_2$ 前驱体生长的影响及其电化学性能

程 磊[1,2]，赵 义[3]，黄 斌[1]，赵早文[4]，李延伟[1]，李 伟[1]

1. 桂林理工大学 化学与生物工程学院 广西电磁化学功能物质重点实验室，桂林 541004；
2. 浙江帕瓦新能源股份有限公司，诸暨 311899；
3. 中南大学 冶金与环境学院，长沙 410083；
4. 海南大学 材料科学与工程学院，海口 570228

摘　要：采用钨掺杂的前驱体为原料合成 $LiNi_{0.88}Co_{0.09}Mn_{0.03}O_2$ 正极材料。X 射线衍射分析表明，钨掺杂可抑制前驱体晶体沿垂直于 c 轴的方向生长。扫描电镜结果表明，随着钨掺杂量的增加，正极材料的一次颗粒粒度呈减小的趋势。电化学表征证实钨掺杂的优势。掺钨量为 0.4%(质量分数)的正极材料相比空白样品具有显著提高的电化学性能，以 10C 电流密度分别在 25 和 45 ℃下循环 100 周后，分别具有 94.68%和 89.63%的容量保持率。同时，钨掺杂还可抑制材料在循环时产生晶间裂纹。因此，得益于钨掺杂对材料成分调节及微观结构调控的协同作用，锂离子在材料中的扩散速率增加，材料的结构稳定性提高。

关键词：钨掺杂；前驱体生长；结构稳定性；循环寿命；锂离子电池

(Edited by Bing YANG)